Numerical Solution of the Upper-Convected Maxwell Model for Three-Dimensional Free Surface Flows

Murilo F. Tomé[1], Renato A. P. Silva[1], Cassio M. Oishi[1]
and Sean McKee[2,*]

[1] *Departamento de Matemática Aplicada e Estatística, Instituto de Ciências Matemáticas e de Computação, Universidade de São Paulo, São Carlos, Brazil.*
[2] *Department of Mathematics, University of Strathclyde, Glasgow, UK.*

Abstract. This work presents a finite difference technique for simulating three-dimensional free surface flows governed by the Upper-Convected Maxwell (UCM) constitutive equation. A Marker-and-Cell approach is employed to represent the fluid free surface and formulations for calculating the non-Newtonian stress tensor on solid boundaries are developed. The complete free surface stress conditions are employed. The momentum equation is solved by an implicit technique while the UCM constitutive equation is integrated by the explicit Euler method. The resulting equations are solved by the finite difference method on a 3D-staggered grid. By using an exact solution for fully developed flow inside a pipe, validation and convergence results are provided. Numerical results include the simulation of the transient extrudate swell and the comparison between jet buckling of UCM and Newtonian fluids.

AMS subject classifications: 76A10, 76D05, 76M20

Key words: Viscoelastic flow, Upper-Convected Maxwell, finite difference, free surface, implicit techniques, Marker-and-Cell.

1 Introduction

A common industrial process is extrusion whereby a complex fluid is passed through a die under pressure. The extrudate, the polymer that exits the die, may be the final product or may be an intermediate stage in the industrial process. Other industrial applications involving complex fluids include container filling and polymer injection. These problems are often time-dependent, non-isothermal, and viscoelastic: they also often

*Corresponding author. *Email addresses:* murilo@icmc.usp.br (M. F. Tomé), silva.renato@gmail.com (R. A. P. Silva), oishi@icmc.usp.br (C. M. Oishi), smck@maths.strath.ac.uk (S. McKee)

have multiple free surfaces and the geometries can be complex. Computational rheology, and in particular viscoelastic free surface flows, has been an active area (see, for example, [1–4, 16, 24, 27, 41, 43] to mention a few). However, much of the work has dealt with two-dimensional, steady state, creeping flows. Notwithstanding, 3D confined flows employing the Upper-Convected Maxwell (UCM), Oldroyd-B, Phan-Thien-Tanner (PTT) models can be found in the literature (eg. [5–10]). More recently, there have been several attempts to model three-dimensional viscoelastic free surface flow: for example, Rassmussen and Hassager [11] used a 3D-Lagrangian integral model to simulate the elastic end-plate instability of polymeric filaments employing the UCM model. Kim et al. [12] developed a finite element code using the Volume-of-Fluid (VOF) technique to simulate 2D/3D free surface flows of Newtonian and Generalized Newtonian (GNF) fluids. Kim's code is in principle capable of dealing with three-dimensional moving free surfaces, but is yet to be tested on real problems. More recently, Bonito et al. [13] presented a finite element/finite volume technique that was capable of solving three-dimensional viscoelastic flows with moving free surfaces. In particular, Bonito et al. [13] presented jet buckling results for both Newtonian and Oldroyd-B fluids.

On the millennium, Castelo et al. [18] developed a fully three-dimensional code called Freeflow3D. In this code the governing equations were solved by the finite difference method on a staggered grid and the free surface(s) modeled by a Marker-and-Cell method [14]. Freeflow3D can deal with time-dependent free surface flows and can cope with multiple moving free surfaces. It can simulate container filling and jet buckling of Newtonian fluids (e.g. Tomé et al. [17]), deal similarly with Generalized Newtonian flows [22], and more recently it has been extended to viscoelastic free surface flows of Oldroyd-B fluids (see Tomé et al. [25]).

In this work we develop a numerical method for simulating three-dimensional viscoelastic free surface flows governed by the Upper-Convected Maxwell constitutive equation. The momentum equations are solved by the implicit Euler method combined with an implicit technique for calculating the pressure on the free surface. The UCM constitutive equation is solved by the explicit Euler scheme. The method is validated by simulating fully developed flow in a 3D-pipe and convergence results are obtained through mesh refinement. Results of fully three-dimensional viscoelastic flows with moving free surfaces are given.

2   Governing equations

Incompressible and isothermal flows are governed by the mass conservation equation and the equation of motion which can be written as

$$\nabla \cdot \mathbf{u} = 0, \tag{2.1}$$

$$\frac{\partial \mathbf{u}}{\partial t} + \nabla \cdot (\mathbf{u}\mathbf{u}) = \frac{1}{\rho}\big[-\nabla p + \nabla \cdot \mathbf{T}\big] + \mathbf{g}, \tag{2.2}$$

where $\mathbf{u} = (u,v,w)^T$ is the velocity vector, t is the time, p is the pressure, ρ is the fluid density, $\mathbf{g} = (g_x, g_y, g_z)^T$ is the gravity field and $\mathbf{T}$ is the extra-stress tensor. In this work the fluid is modeled by the UCM constitutive equation

$$\mathbf{T} + \lambda \overset{\triangledown}{\mathbf{T}} = 2\mu \mathbf{D}, \tag{2.3}$$

where $\mathbf{D} = \frac{1}{2}\left[\nabla \mathbf{u} + (\nabla \mathbf{u})^T\right]$ is the rate of deformation tensor, μ is the fluid viscosity, λ is the relaxation-time of the fluid and $\overset{\triangledown}{\mathbf{T}}$ is the upper-convected derivative of $\mathbf{T}$ defined by

$$\overset{\triangledown}{\mathbf{T}} = \frac{\partial \mathbf{T}}{\partial t} + \nabla \cdot (\mathbf{u}\mathbf{T}) - (\nabla \mathbf{u})^T \cdot \mathbf{T} - \mathbf{T} \cdot (\nabla \mathbf{u}).$$

To solve Eqs. (2.1)-(2.3) we employ EVSS method [26]

$$\mathbf{T} = \mathbf{S} + 2\mu \mathbf{D}, \tag{2.4}$$

where $\mathbf{S}$ is a non-Newtonian tensor responsible for the non-Newtonian contribution to the extra-stress tensor. The principal reason for this choice is to stabilize the numerical scheme: in principle (2.3) could be solved directly, avoiding the introduction of $\mathbf{S}$, but this leads to an unstable scheme even for very moderate values of the Weissenberg number.

We shall employ a non-dimensional form where

$$\bar{\mathbf{x}} = \frac{1}{L}\mathbf{x}, \quad \bar{t} = \frac{U}{L}t, \; \bar{\mathbf{u}} = \frac{1}{U}\mathbf{u}, \quad \bar{p} = \frac{1}{\rho U^2}p, \quad \bar{\mathbf{g}} = \frac{1}{g}\mathbf{g}, \quad \bar{\mathbf{S}} = \frac{1}{\rho U^2}\mathbf{S}.$$

Using (2.4), $\mathbf{T}$ is eliminated from Eqs. (2.2) and (2.3) and the resulting equations are nondimensionalized. Upon omitting the bars for clarity Eq. (2.1) remains unchanged while Eqs. (2.2) and (2.3) become

$$\frac{\partial \mathbf{u}}{\partial t} = -\nabla \cdot (\mathbf{u}\mathbf{u}) - \nabla p + \frac{1}{Re}\nabla^2 \mathbf{u} + \nabla \cdot \mathbf{S} + \frac{1}{Fr^2}\mathbf{g}, \tag{2.5}$$

$$\frac{\partial \mathbf{S}}{\partial t} = -\frac{1}{We}\mathbf{S} - \nabla \cdot (\mathbf{u}\mathbf{S}) + (\nabla \mathbf{u})^T \cdot \mathbf{S} + \mathbf{S} \cdot (\nabla \mathbf{u})$$
$$- \frac{2}{Re}\left[\frac{\partial \mathbf{D}}{\partial t} + \nabla \cdot (\mathbf{u}\mathbf{D}) - (\nabla \mathbf{u})^T \cdot \mathbf{D} - \mathbf{D} \cdot (\nabla \mathbf{u})\right], \tag{2.6}$$

where $Re = \rho UL/\mu$, $We = \lambda U/L$ and $Fr = U/\sqrt{Lg}$ are the Reynolds, Weissenberg and Froude numbers, respectively. We consider three-dimensional Cartesian flows so that the mass conservation equation (2.1) together with the equation of motion (2.5) and the constitutive equation (2.6) consist of a system with ten equations for the unknowns u, v, w, p, S^{xx}, S^{xy}, S^{xz}, S^{yy}, S^{yz} and S^{zz}. The mass equation (2.1) becomes

$$\frac{\partial u}{\partial x} + \frac{\partial v}{\partial y} + \frac{\partial w}{\partial z} = 0, \tag{2.7}$$

and the first components of Eqs. (2.5) and (2.6) are written, respectively, as

$$
\frac{\partial u}{\partial t} = -\frac{\partial (u^2)}{\partial x} - \frac{\partial (vu)}{\partial y} - \frac{\partial (wu)}{\partial z}
$$
$$
-\frac{\partial p}{\partial x} + \frac{1}{Re}\left(\frac{\partial^2 u}{\partial x^2} + \frac{\partial^2 u}{\partial y^2} + \frac{\partial^2 u}{\partial z^2}\right) + \frac{\partial S^{xx}}{\partial x} + \frac{\partial S^{xy}}{\partial y} + \frac{\partial S^{xz}}{\partial z} + \frac{1}{Fr^2}g_x, \tag{2.8}
$$
$$
\frac{\partial S^{xx}}{\partial t} = -\frac{\partial (uS^{xx})}{\partial x} - \frac{\partial (vS^{xx})}{\partial y} - \frac{\partial (wS^{xx})}{\partial z} + 2\left(\frac{\partial u}{\partial x}S^{xx} + \frac{\partial u}{\partial y}S^{xy} + \frac{\partial u}{\partial z}S^{xz}\right)
$$
$$
-\frac{1}{We}S^{xx} - \frac{2}{Re}\left[\frac{\partial D^{xx}}{\partial t} + \frac{\partial (uD^{xx})}{\partial x} + \frac{\partial (vD^{xx})}{\partial y} + \frac{\partial (wD^{xx})}{\partial z}\right.
$$
$$
\left. -2\left(\frac{\partial u}{\partial x}D^{xx} + \frac{\partial u}{\partial y}D^{xy} + \frac{\partial u}{\partial z}D^{xz}\right)\right]. \tag{2.9}
$$

The other components of both Eqs. (2.5) and (2.6) are written in a similar manner.

Eqs. (2.1), (2.5) and (2.6) will be solved within the framework of the GENSMAC3D method [17] (see also Castelo et al. [18]). A staggered grid is used and a strategy for the classification of the cells within the mesh is employed to track the moving free surface. Fig. 1(a) illustrates this classification for a two-dimensional flow while Fig. 1(b) displays a typical cell of the mesh. In the present work, the same cell classification is used, that is

---

- Empty Cell (E): Cells that do not contain fluid;
- Full Cell(F): Cells that contain fluid and do not possess any faces in contact with empty cell faces;
- Surface Cell (S): Cells that contain fluid and necessarily have faces in contact with empty cell faces;
- Boundary Cell (B): Cells that define the positions of rigid boundaries;
- Inflow Cell (I): Cells that define entrance of the fluid (inflow);
- Outflow Cell (O): Cells that define exit of the fluid (outflow).

The free surface is approximated by a piecewise linear surface composed of triangles and quadrilaterals that contain marker particles on their vertices. It may happen that two vertices may become too far away or too close to each other so that a scheme for inserting and deleting particles (creating/deleting (new) triangles and quadrilaterals) is employed. For details see Castelo et al. [18].

One point should perhaps be made. The UCM model can be obtained from the Oldroyd-B model by letting the retardation time parameter λ_2 tend to zero and it might therefore be felt that in view of the author's previous work on the 3D Oldroyd-B model [25] that this work is redundant. This is not the case. Due to the EVSS transformation $\mathbf{T} = \mathbf{S} + 2\mu\mathbf{D}$ (employed to simplify the Oldroyd B constitutive equation), the boundary
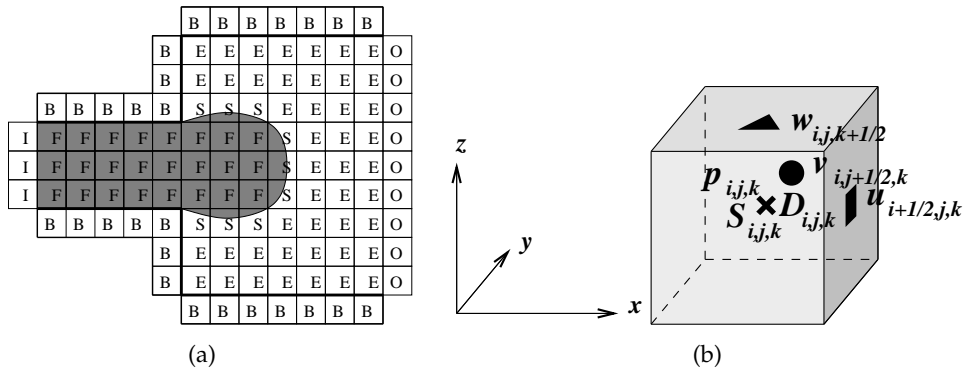
Figure 1: (a) Types of cells used by GENSMAC3D; (b) Three-dimensional staggered grid used.

conditions on the free surface involve the ratio λ_1/λ_2 which precludes any possibility of letting $\lambda_2=0$ in the existing code.

3　Boundary conditions

To solve Eqs. (2.1), (2.5) and (2.6), boundary conditions are required. Let the subscripts n, t_1 and t_2 denote normal and tangential components to the boundary, respectively. Then, for the velocity vector **u** we impose no-slip conditions on solid boundaries (**u** $=$ **0**); at fluid entrances (inflows) the velocity is specified by $u_n = U_{inf}$ and $u_{t_1} = u_{t_2} = 0$, where U_{inf} is a function which defines a constant or a paraboloidal profile along the inflow; at fluid exits (outflows) we adopt the homogeneous Neumann conditions

$$\frac{\partial u_n}{\partial n} = \frac{\partial u_{t_1}}{\partial n} = \frac{\partial u_{t_2}}{\partial n} = 0.$$

3.1　Free surface stress conditions

We consider a viscous fluid flowing into a passive atmosphere and assume that surface tension forces can be neglected. Thus, on the moving free surface the correct boundary conditions are (see Batchelor [28], p. 153)

$$\mathbf{n}\cdot(\boldsymbol{\tau}\cdot\mathbf{n})=0, \tag{3.1}$$

$$\mathbf{m}_1\cdot(\boldsymbol{\tau}\cdot\mathbf{n})=0, \tag{3.2}$$

$$\mathbf{m}_2\cdot(\boldsymbol{\tau}\cdot\mathbf{n})=0, \tag{3.3}$$

where **n** is the outward unit normal vector and $\mathbf{m}_1$ and $\mathbf{m}_2$ are unit tangential vectors to the free surface. The tensor $\boldsymbol{\tau}$ is the stress tensor (written in the non-dimensional form) given by $\boldsymbol{\tau} = -p\mathbf{I}+\mathbf{S}+\frac{2}{Re}\mathbf{D}$.

Eqs. (3.1)-(3.3) represent the appropriate boundary conditions at a fluid free surface. It is known that three-dimensional free surface flows are highly affected by the manner in which these conditions are applied. However, several authors approximate the normal stress condition (3.1) simply by setting $p\!=\!0$ (e.g. [29–31]). This could be used only in the case of Newtonian flows possessing $Re\!\gg\!1$. The tangential conditions have usually been ignored (see, e.g., [29]).

To apply the conditions above we follow the ideas presented in Tomé et al. [17]. It is supposed that the mesh spacing is sufficiently small that the free surface can be locally approximated by a planar surface. Following Tomé et al., three cases are considered.

i) 1D planar surfaces parallel to one co-ordinate axis. These surfaces are identified by S-cells having only one face in contact with an E-cell face.

ii) 2D planar surfaces are assumed to make 45° with two co-ordinate axes and are recognized by S-cells having two adjacent faces in contact with E-cell faces.

iii) 3D planar surfaces are considered to be surfaces that make 60° with three co-ordinate axes and are represented by S-cells having three adjacent faces in contact with E-cell faces. Fig. 2 displays an example of 1D, 2D and 3D planar surfaces.

By using these three types of approximations for the free surface, the normal stress condition (3.1) is used to compute the pressure on the free surface while the tangential stress conditions, Eqs. (3.2) and (3.3), are employed to calculate the velocities at the empty cells. For details see [17].
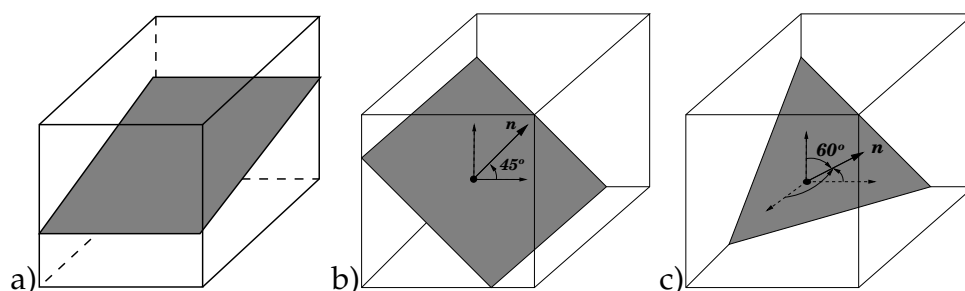
Figure 2: Types of planar surfaces: a) **1D-planar** surface; b) **2D-planar** surface; c) **3D-planar** surface.

4　Numerical method

The numerical method for solving Eqs. (2.1) and (2.5) will be based on the projection method (introduced by Chorin [33]) while the constitutive equation (2.6) is approximated by a second order finite difference method on a staggered grid (Fig. 1b). The fluid is modeled by the Marker-and-Cell method [14] that employs marker particles to track the moving free surface (for more details see Tomé et al. [17]).

In this work, the velocity and the pressure are obtained by implicitly solving the momentum equation (2.5) for an intermediate velocity field followed by the solution of an elliptic equation to conserve mass (2.1).

There are several ways to solve (2.1) and (2.5) using implicit techniques (e.g., [34–37]). However, we are interested in low Reynolds number viscoelastic free surface flows so that the convective terms of the momentum equations are not so crucial. The non-Newtonian stress tensor $\mathbf{S}$ is calculated by a hyperbolic equation and $\nabla \cdot \mathbf{S}$ is treated as a source term. Thus, if we use the Euler implicit method for the viscous term then Eqs. (2.5) and (2.1) can be written in the form

$$\frac{\mathbf{u}^{(n+1)}}{\delta t} - \frac{1}{Re}\nabla^2 \mathbf{u}^{(n+1)} = \frac{\mathbf{u}^{(n)}}{\delta t} - \nabla \cdot (\mathbf{uu})^{(n)} - \nabla p^{(n+1)} + \nabla \cdot \mathbf{S}^{(n)} + \frac{1}{Fr^2}\mathbf{g}, \qquad (4.1)$$

$$\nabla \cdot \mathbf{u}^{(n+1)} = 0. \qquad (4.2)$$

To uncouple the velocity and pressure fields in Eqs. (4.1) and (4.2) we apply the projection method as follows.

First, we solve Eq. (4.1) for a provisional velocity field $\widetilde{\mathbf{u}}$

$$\frac{\widetilde{\mathbf{u}}}{\delta t} - \frac{1}{Re}\nabla^2 \widetilde{\mathbf{u}} = \frac{\mathbf{u}^{(n)}}{\delta t} - \nabla \cdot (\mathbf{uu})^{(n)} - \nabla p^{(n)} + \nabla \cdot \mathbf{S}^{(n)} + \frac{1}{Fr^2}\mathbf{g}, \qquad (4.3)$$

where the boundary conditions for $\widetilde{\mathbf{u}}$ are the same as for $\mathbf{u}^{(n)}$, and $p^{(n)}$ represents the pressure at time $t = t_n$. The velocity field can be decomposed as

$$\mathbf{u}^{(n+1)} = \widetilde{\mathbf{u}} - \delta t \nabla \psi^{(n+1)}. \qquad (4.4)$$

Taking the divergence of Eq. (4.4) and imposing mass conservation for $\mathbf{u}^{(n+1)}$, one obtains the following Poisson equation for $\psi^{(n+1)}$

$$\nabla^2 \psi^{(n+1)} = \frac{1}{\delta t}\nabla \cdot \widetilde{\mathbf{u}}. \qquad (4.5)$$

This equation is solved in the fluid region and is applied at each full cell F within the mesh. The equations for $\psi^{(n+1)}$ on the free surface are discussed in the next section.

The pressure is calculated by the accurate pressure correction method

$$p^{(n+1)} = p^{(n)} + \psi^{(n+1)} - \frac{\delta t}{2Re}\nabla^2 \psi^{(n+1)}, \qquad (4.6)$$

presented in [38].

After calculating the velocity and pressure, the non-Newtonian tensor $\mathbf{S}$ is obtained by solving the UCM equation (2.6) by the explicit Euler method, namely,

$$\mathbf{S}^{(n+1)} = \mathbf{S}^{(n)} - \frac{\delta t}{We}\mathbf{S}^{(n)} - \delta t \left[\nabla \cdot \left(\mathbf{u}^{(n+1)}\mathbf{S}^{(n)} \right) - \left(\nabla \mathbf{u}^{(n+1)} \right)^T \mathbf{S}^{(n)} - \mathbf{S}^{(n)} \left(\nabla \mathbf{u}^{(n+1)} \right) \right]$$
$$- \frac{2\delta t}{Re} \left[\nabla \cdot (\mathbf{uD})^{(n+1)} - \left((\nabla \mathbf{u})^T \mathbf{D} \right)^{(n+1)} - \left(\mathbf{D}(\nabla \mathbf{u}) \right)^{(n+1)} \right], \qquad (4.7)$$

where $\mathbf{D}^{(n+1)} = \frac{1}{2} \left[\nabla \mathbf{u}^{(n+1)} + (\nabla \mathbf{u}^{(n+1)})^T \right]$.

Eq. (4.7) is a discretization of (2.5) (which is hyperbolic in nature) and as such is subject to the CFL restriction. However, this restriction is considerably less severe than the viscous restriction and consequently any time-step that can be employed for the (implicit) momentum equation (4.1) can also be used for Eq. (2.5).

Thus, the velocity and the pressure field are obtained by solving Eqs. (4.3)-(4.6) while the non-Newtonian tensor **S** is calculated by (4.7).

4.1 Implicit formulation for the pressure at the free surface

In previous works (e.g. [17, 22, 39]), the Navier-Stokes equations were solved by the explicit Euler method and the pressure was calculated explicitly using Eq. (3.1) so that $\psi^{(n+1)}$ was set to zero on the free surface cells. If we assume a uniform mesh with $\delta x = \delta y = \delta z = h$, then the explicit solution of the Navier-Stokes imposes the following restriction on the time-step to be employed in the calculation

$$\delta t < Re \frac{\delta h^2}{6}. \tag{4.8}$$

However, polymer flows usually involve low Reynolds number ($Re \ll 1$)) in which case condition (4.8) leads to very small time-steps which makes the calculation very inefficient. To overcome this restriction, Oishi et al. [40] presented a two-dimensional numerical technique using the implicit Euler method to solve the provisional velocity field together with a methodology to calculate the pressure on the free surface using an implicit technique. More recently, the ideas of Oishi et al. [40] were extended to three-dimensional flows of Newtonian and Oldroyd-B fluids (see Oishi et al. [38]) and good results were reported. Therefore, we follow the ideas of Oishi et al. [38] and solve the equations for the pressure at the free surface using Eq. (3.1) which will be treated implicitly. The tangential conditions given by Eqs. (3.2) and (3.3) are discretized explicitly as in GENSMAC3D [17] (see also Tomé et al. [25]). By using Cartesian coordinates, the normal stress condition, Eq. (3.1), can then be written as

$$
\begin{aligned}
p^{(n+1)} = \frac{2}{Re} \Bigg[& \frac{\partial u}{\partial x} n_x^2 + \frac{\partial v}{\partial y} n_y^2 + \frac{\partial w}{\partial z} n_z^2 + \left(\frac{\partial v}{\partial x} + \frac{\partial u}{\partial y} \right) n_x n_y \\
& + \left(\frac{\partial w}{\partial x} + \frac{\partial u}{\partial z} \right) n_x n_z + \left(\frac{\partial w}{\partial y} + \frac{\partial v}{\partial z} \right) n_y n_z \Bigg]^{(n+1)} \\
& + \left[S^{xx} n_x^2 + S^{yy} n_y^2 + S^{zz} n_z^2 + 2 (S^{xy} n_x n_y + S^{xz} n_x n_z + S^{yz} n_y n_z) \right]^{(n)}.
\end{aligned}
\tag{4.9}
$$

We point out that this equation couples the velocity and the pressure and a strategy for decoupling them was essential for the algorithm to be competitive. The strategy we adopted uses the equation for the corrected velocity and the pressure (see Eqs. (4.4) and (4.6)) to construct new equations for the (added velocity) potential $\psi^{(n+1)}$ at the free surface. To demonstrate how this can be done let us consider the case of a S-cell with the
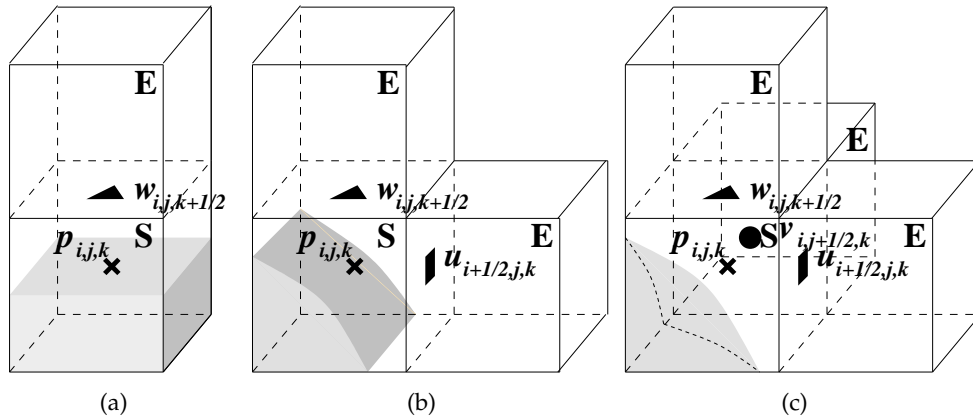
Figure 3: **a**) The normal vector is pointing to the z-direction; **b**) The normal vector is making 45° with the z- and x- co-ordinate axes; **c**) The normal vector is making 60° with the x-, y- and z- co-ordinate axes.

$(k+\frac{1}{2})$-face in contact with an E-cell face as shown in Fig. 3(a). For this cell we assume the surface is of type 1D-planar and the normal vector is $\mathbf{n}=(0,0,1)$. In this case, Eq. (4.9) reduces to

$$p^{(n+1)} = \frac{2}{Re}\left(\frac{\partial w^{(n+1)}}{\partial z}\right) + (S^{zz})^{(n)}. \tag{4.10}$$

Now, the mass conservation Eq. (2.7) discretized at time level $(n+1)$ gives

$$\frac{\partial w^{(n+1)}}{\partial z} = -\frac{\partial u^{(n+1)}}{\partial x} - \frac{\partial v^{(n+1)}}{\partial y}, \tag{4.11}$$

and introducing it into Eq. (4.10) leads to

$$p^{(n+1)} = -\frac{2}{Re}\left(\frac{\partial u^{(n+1)}}{\partial x} + \frac{\partial v^{(n+1)}}{\partial y}\right) + (S^{zz})^{(n)}. \tag{4.12}$$

Eq. (4.4), written in component form, yields

$$\begin{cases} u^{(n+1)} = \widetilde{u} - \delta t \dfrac{\partial \psi^{(n+1)}}{\partial x}, \\[2mm] v^{(n+1)} = \widetilde{v} - \delta t \dfrac{\partial \psi^{(n+1)}}{\partial y}, \\[2mm] w^{(n+1)} = \widetilde{w} - \delta t \dfrac{\partial \psi^{(n+1)}}{\partial z}, \end{cases} \tag{4.13}$$

so that introducing $u^{(n+1)}$ and $v^{(n+1)}$ into Eq. (4.12) we obtain

$$p^{(n+1)} = \frac{2}{Re}\left(\delta t\frac{\partial^2 \psi^{(n+1)}}{\partial x^2} + \delta t\frac{\partial^2 \psi^{(n+1)}}{\partial y^2} - \frac{\partial \widetilde{u}}{\partial x} - \frac{\partial \widetilde{v}}{\partial y}\right) + (S^{zz})^{(n)}. \tag{4.14}$$

Finally, substituting $p^{(n+1)}$ from Eq. (4.6) into Eq. (4.14) and regrouping the terms we obtain the following equation for the potential $\psi^{(n+1)}$

$$\psi^{(n+1)} - \frac{\delta t}{2Re} \nabla^2 \psi^{(n+1)} - \frac{2\delta t}{Re} \left(\frac{\partial^2 \psi^{(n+1)}}{\partial x^2} + \frac{\partial^2 \psi^{(n+1)}}{\partial y^2} \right)$$
$$= -\frac{2}{Re} \left(\frac{\partial \widetilde{u}}{\partial x} + \frac{\partial \widetilde{v}}{\partial y} \right) - p^{(n)} + (S^{zz})^{(n)}. \tag{4.15}$$

The cases of 1D-planar surfaces with $\mathbf{n} = (0, \pm 1, 0)$ and $\mathbf{n} = (\pm 1, 0, 0)$ are dealt with similarly.

2D-planar surfaces are identified by surface cells with two adjacent faces in contact with empty cell faces (e.g. Fig. 3(b) displays a case of 2D-planar surface with $\mathbf{n} = \left(\frac{\sqrt{2}}{2}, 0, \frac{\sqrt{2}}{2} \right)$) while 3D-planar surfaces are identified by surface cells with three adjacent faces in contact with empty cell faces (see Fig. 3(c) for the case of a 3D-planar surface with $\mathbf{n} = \left(\frac{\sqrt{3}}{3}, \frac{\sqrt{3}}{3}, \frac{\sqrt{3}}{3} \right)$).

The derivation of the equations for $\psi^{(n+1)}$ corresponding to 2D- and 3D-planar surfaces is rather lengthy and it has been fully detailed in Oishi et al. [38]; for this reason it is not presented here.

4.2 Algorithm

To solve the numerical method outlined in Sections 4 and 4.1 we employ the following algorithm.

It is supposed that at time t_n, the solenoidal-velocity field $\mathbf{u}^{(n)}$ and $\mathbf{S}^{(n)}$ are known and suitable boundary conditions for the velocity and pressure are given. The updated velocity field $\mathbf{u}^{(n+1)}$, the pressure field $p^{(n+1)}$ and the non-Newtonian stress tensor $\mathbf{S}^{(n+1)}$ at time $t_{n+1} = t_n + \delta t$ are calculated sequentially by Algorithm 4.1.

4.3 Basic finite difference equations

We present the finite difference approximations corresponding to the equations of the computational algorithm outlined in the previous sub-section.

The momentum equation, Eq. (4.3), is approximated as follows: the time derivative and the viscous terms are approximated by the implicit Euler method while the pressure gradient and the divergence of the non-Newtonian stress tensor **S** are discretized using central differences at the previous time level. The convective terms are calculated by the high order upwind scheme CUBISTA (Convergent Universally Bounded Interpolation Scheme for the Treatment of Advection) of Alves et al. [41]. The CUBISTA scheme is third order accurate on a uniform mesh for smooth flows, but its real strength is its bounded nature which ensures stability. Details of the finite difference equations for the CUBISTA method can be found in [42]. For instance, the x-component of the momentum equation

Algorithm 4.1:

Step 1: Calculate the intermediate velocity field $\widetilde{\mathbf{u}}^{(n+1)}$ from Eq. (4.3) implicitly using the Euler implicit method. The resulting symmetric linear system is solved by the conjugate gradient method.
Step 2: Solve the Poisson equation (4.5) together with the equations derived for the potential function $\psi^{(n+1)}$ at the free surface (see Section 4.1). The appropriate boundary conditions for these equations are $\psi^{(n+1)}=0$ on outflows while the homogeneous Neumann condition is used for fixed boundaries and inflows. The resulting linear system for $\psi^{(n+1)}$ is sparse and non-symmetric: we therefore employ the bi-conjugated gradient method with diagonal (known as Jacobi) pre-conditioning to solve this linear system. The corresponding finite difference equations will be given in the next section.
Step 3: Compute the final velocity $\mathbf{u}^{(n+1)}$ from (4.4).
Step 4: Compute the pressure from (4.6).
Step 5: Calculate the stress tensor $\mathbf{S}^{(n+1)}$ from Eq. (4.7). This equation is solved by explicit finite differences which are given in the next section.
Step 6: Update the positions of the marker particles by solving

$$\dot{\mathbf{x}} = \mathbf{u}^{(n+1)}, \tag{4.16}$$

by the explicit Euler's method.

---

is approximated by the following difference equation

$$
\begin{aligned}
&\left[1+\left(\frac{2\delta t}{Re}\right)\left(\frac{1}{\delta x^2}+\frac{1}{\delta y^2}+\frac{1}{\delta z^2}\right)\right]\widetilde{u}_{i+\frac{1}{2},j,k}-\left(\frac{\delta t}{Re\delta x^2}\right)\left(\widetilde{u}_{i+\frac{3}{2},j,k}+\widetilde{u}_{i-\frac{1}{2},j,k}\right)\\
&\quad-\left(\frac{\delta t}{Re\delta y^2}\right)\left(\widetilde{u}_{i+\frac{1}{2},j+1,k}+\widetilde{u}_{i+\frac{1}{2},j-1,k}\right)-\left(\frac{\delta t}{Re\delta z^2}\right)\left(\widetilde{u}_{i+\frac{1}{2},j,k+1}+\widetilde{u}_{i+\frac{1}{2},j,k-1}\right)\\
&=u^{(n)}_{i+\frac{1}{2},j,k}+\delta t\left\{-\left(\mathcal{C}(uu)+\mathcal{C}(vu)+\mathcal{C}(wu)\right)^{(n)}-\left(\frac{p_{i+1,j,k}-p_{i,j,k}}{\delta x}\right)^{(n)}\right.\\
&\quad\left.+\left[\frac{S^{xx}_{i+1,j,k}-S^{xx}_{i,j,k}}{\delta x}+\frac{S^{yx}_{i+\frac{1}{2},j+\frac{1}{2},k}-S^{yx}_{i+\frac{1}{2},j-\frac{1}{2},k}}{\delta y}+\frac{S^{zx}_{i+\frac{1}{2},j,k+\frac{1}{2}}-S^{zx}_{i+\frac{1}{2},j,k-\frac{1}{2}}}{\delta z}\right]^{(n)}+\frac{1}{Fr^2}g_x\right\}, \quad (4.17)
\end{aligned}
$$

where the convective terms $\mathcal{C}(uu)$, $\mathcal{C}(vu)$ and $\mathcal{C}(wu)$ are approximated by the CUBISTA method. Terms like $S^{yx}_{i+\frac{1}{2},j+\frac{1}{2},k}$ are obtained by averaging its nearest neighbours, for instance,

$$
S^{yx}_{i+\frac{1}{2},j+\frac{1}{2},k}=\frac{1}{4}\left(S^{yx}_{i,j,k}+S^{yx}_{i+1,j,k}+S^{yx}_{i,j+1,k}+S^{yx}_{i+1,j+1,k}\right).
$$

The y- and z-components of the momentum equation are obtained in the same way. Therefore, the calculation of the provisional velocity field $\widetilde{\mathbf{u}}$ leads to the solution of three sparse symmetric linear systems which are solved by the conjugate gradient method. The implementation of the conjugate gradient solver follows the ideas presented by Tomé and McKee [15].

4.3.1   Calculation of the potential function $\psi^{(n+1)}$

The Poisson equation (4.5) is discretized by the following second order difference equation

$$
\frac{\psi_{i+1,j,k}^{(n+1)} - 2\psi_{i,j,k}^{(n+1)} + \psi_{i-1,j,k}^{(n+1)}}{\delta x^2} + \frac{\psi_{i,j+1,k}^{(n+1)} - 2\psi_{i,j,k}^{(n+1)} + \psi_{i,j-1,k}^{(n+1)}}{\delta y^2} + \frac{\psi_{i,j,k+1}^{(n+1)} - 2\psi_{i,j,k}^{(n+1)} + \psi_{i,j,k-1}^{(n+1)}}{\delta z^2}
$$

$$
= \frac{1}{\delta t}\left(\frac{\widetilde{u}_{i+\frac{1}{2},j,k} - \widetilde{u}_{i-\frac{1}{2},j,k}}{\delta x} + \frac{\widetilde{v}_{i,j+\frac{1}{2},k} - \widetilde{v}_{i,j-\frac{1}{2},k}}{\delta y} + \frac{\widetilde{w}_{i,j,k+\frac{1}{2}} - \widetilde{w}_{i,j,k-\frac{1}{2}}}{\delta z} \right). \tag{4.18}
$$

Eq. (4.18) is applied at each full cell in the domain. The calculation of $\psi_{i,j,k}^{(n+1)}$ on surface cells is carried out following the ideas detailed in Section 4.1 with the corresponding equations for each type of surface, i.e., 1D, 2D or 3D-planar surfaces.

The resulting linear system composed by the Poisson equation Eq. (4.18) applied to the full cells together with the equations obtained for $\psi_{i,j,k}^{(n+1)}$ in the surface cells, is sparse and non-symmetric. We apply the Bi-conjugate gradient method with Jacobi preconditioning to solve this linear system.

4.4   Solution of the constitutive equation

The constitutive equation Eq. (4.7) is approximated by second order finite differences and applied at the centre of each full cell F and each surface cell S. The time derivative is discretized by the explicit Euler method while the spatial derivatives are second order approximated. The advective terms are calculated using a high order upwind scheme. In this work we employ the CUBISTA method presented by Alves et al. [41] (see next section, Section 4.5). For example, the S^{xx} component of Eq. (4.7) is calculated by the following difference equations

$$
\left(S_{i,j,k}^{xx}\right)^{(n+1)} = \left(S_{i,j,k}^{xx}\right)^{(n)} - \frac{\delta t}{We}\left(S_{i,j,k}^{xx}\right)^{(n)} - \delta t\Big\{ \mathcal{C}\left[u^{n+1}(S^{xx})^{(n)}\right]_{i,j,k} + \mathcal{C}\left[v^{n+1}(S^{xx})^{(n)}\right]_{i,j,k}
$$

$$
+ \mathcal{C}\left[w^{n+1}(S^{xx})^{(n)}\right]_{i,j,k} + 2\left[\left(\frac{\partial u^{(n+1)}}{\partial x}(S^{xx})^{(n)}\right)_{i,j,k} + \left(\frac{\partial u^{(n+1)}}{\partial y}(S^{xy})^{(n)}\right)_{i,j,k}\right.
$$

$$
+ \left(\frac{\partial u^{(n+1)}}{\partial z}(S^{xz})^{(n)}\right)_{i,j,k}\Bigg] - \frac{2}{Re}\left(\left[\mathcal{C}(uD^{xx})_{i,j,k}\right]^{(n+1)} + \left[\mathcal{C}(vD^{xx})_{i,j,k}\right]^{(n+1)} + \left[\mathcal{C}(wD^{xx})_{i,j,k}\right]^{(n+1)} \right.
$$

$$
+ 2\left[\left(\frac{\partial u}{\partial x}D^{xx}\right)_{i,j,k}^{(n+1)} + \left(\frac{\partial u}{\partial y}D^{xy}\right)_{i,j,k}^{(n+1)} + \left(\frac{\partial u}{\partial z}D^{xz}\right)_{i,j,k}^{(n+1)}\right]\right)\Big\}, \tag{4.19}
$$

where the advective terms

$$
\mathcal{C}\left[u^{(n+1)}(S^{xx})^{(n)}\right]_{i,j,k} = \left[\frac{\partial u^{(n+1)}(S^{xx})^{(n)}}{\partial x}\right]_{i,j,k}, \cdots, \left[\mathcal{C}(wD^{xx})^{(n+1)}\right]_{i,j,k} = \left[\frac{\partial w^{(n+1)}(D^{xx})^{(n)}}{\partial z}\right]_{i,j,k}
$$

are calculated by the CUBISTA method. The first-order derivatives are approximated by central differences except at points that are adjacent to a boundary where a forward/backward difference is employed.

The other components of the constitutive equation are obtained by a similar difference equation.

4.5 Calculation of the non-Newtonian tensor S on mesh boundaries
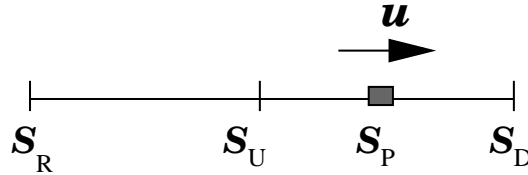
Figure 4: Reference points used by the high order CUBISTA upwind scheme.

The high order upwind CUBISTA [41] requires the values of a variable, for instance **S**, be positioned upstream ($\mathbf{S}_U$), downstream $\mathbf{S}_D$ and remote-upstream $\mathbf{S}_R$ with respect to the point at which the variable is being approximated (see Fig. 4). Therefore, when computing the advective terms $\nabla \cdot \left(\mathbf{u}^{(n+1)} \mathbf{S}^{(n)} \right)$ and $\nabla \cdot \left(\mathbf{u} \mathbf{D} \right)^{(n+1)}$ of Eq. (4.7) at mesh points which are near the boundary domain, the values of the non-Newtonian tensor **S** and the rate of deformation tensor **D** on the mesh boundaries are required. The rate of deformation tensor **D** is easily calculated by

$$\mathbf{D}^{(n+1)} = \frac{1}{2} \left[\nabla \mathbf{u}^{(n+1)} + (\nabla \mathbf{u}^{(n+1)})^T \right]. \tag{4.20}$$

For the non-Newtonian tensor **S** we adopt the strategy employed by Crochet et al. [27] and Mompean and Deville [10]: on inflows we have $\mathbf{S} = \mathbf{0}$ and on outflows the homogeneous Neumann condition $\partial \mathbf{S} / \partial n = \mathbf{0}$ is adopted.

To compute the non-Newtonian tensor **S** on rigid boundaries we follow the ideas of Tomé et al. [43]. First we introduce the change of variables $\mathbf{S} = e^{-\frac{1}{We}t} \widetilde{\mathbf{S}}$ into Eq. (2.6) to obtain (assuming that the no-slip condition holds on rigid boundaries)

$$\frac{\partial \widetilde{\mathbf{S}}}{\partial t} = (\nabla \mathbf{u})^T \widetilde{\mathbf{S}} + \widetilde{\mathbf{S}} (\nabla \mathbf{u}) + \frac{2}{Re} e^{\frac{1}{We}t} \left[(\nabla \mathbf{u})^T \mathbf{D} + \mathbf{D} (\nabla \mathbf{u}) \right]. \tag{4.21}$$

In this work we consider rigid boundaries that are represented by planes that are orthogonal to one of the three coordinate axes (see Fig. 5). Thus, in three dimensions the rigid boundaries can be represented by six planes. For instance, if we consider rigid boundaries orthogonal to the z-axis, ie. parallel to xy-plane (see Fig. 5(a)), then there are two types of rigid boundaries, one that has the normal vector pointing to the positive z-direction and the other that has the normal vector pointing to the negative z-direction.
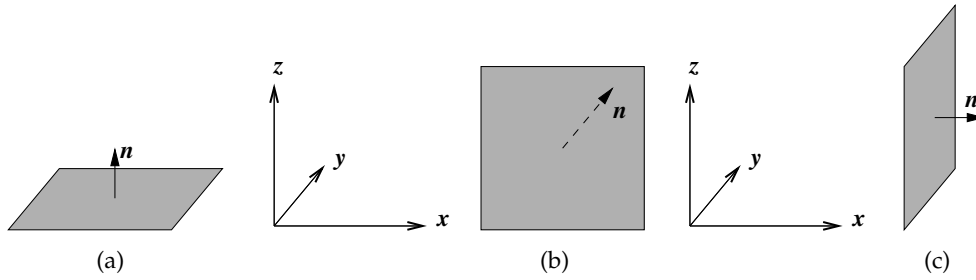
Figure 5: Rigid boundaries parallel to xy- (a), xz- (b) and yz-planes (c).

The components of the non-Newtonian tensor **S** are obtained as follows. By considering rigid boundaries which are parallel to the xy-plane (Fig. 5(a)), the no-slip condition applied to the velocity field produces

$$\frac{\partial u}{\partial x} = \frac{\partial v}{\partial x} = \frac{\partial w}{\partial x} = 0, \quad \frac{\partial u}{\partial y} = \frac{\partial v}{\partial y} = \frac{\partial w}{\partial y} = 0,$$

and finally, applying the mass conservation equation (2.7) we get $\partial w / \partial z = 0$. Therefore, the components of the rate of deformation tensor reduce to

$$D^{xx} = D^{xy} = D^{yy} = D^{zz} = 0, \quad D^{xz} = \frac{1}{2}\frac{\partial u}{\partial z}, \quad D^{yz} = \frac{1}{2}\frac{\partial v}{\partial z}.$$

In this case, the components of Eq. (4.21) can be written as

$$\frac{\partial \widetilde{S}^{xx}}{\partial t} = 2\frac{\partial u}{\partial z}\widetilde{S}^{xz} + \frac{2}{Re}e^{\frac{1}{We}t}\left(\frac{\partial u}{\partial z}\right)^2, \tag{4.22}$$

$$\frac{\partial \widetilde{S}^{yy}}{\partial t} = 2\frac{\partial v}{\partial z}\widetilde{S}^{yz} + \frac{2}{Re}e^{\frac{1}{We}t}\left(\frac{\partial v}{\partial z}\right)^2, \tag{4.23}$$

$$\frac{\partial \widetilde{S}^{zz}}{\partial t} = 0, \tag{4.24}$$

$$\frac{\partial \widetilde{S}^{xy}}{\partial t} = \frac{\partial u}{\partial z}\widetilde{S}^{yz} + \frac{\partial v}{\partial z}\widetilde{S}^{xz} + \frac{2}{Re}e^{\frac{1}{We}t}\left(\frac{\partial u}{\partial z}\frac{\partial v}{\partial z}\right), \tag{4.25}$$

$$\frac{\partial \widetilde{S}^{xz}}{\partial t} = \frac{\partial u}{\partial z}\widetilde{S}^{zz} - \frac{1}{Re}e^{\frac{1}{We}t}\frac{\partial}{\partial t}\left(\frac{\partial u}{\partial z}\right), \tag{4.26}$$

$$\frac{\partial \widetilde{S}^{yz}}{\partial t} = \frac{\partial v}{\partial z}\widetilde{S}^{zz} - \frac{1}{Re}e^{\frac{1}{We}t}\frac{\partial}{\partial t}\left(\frac{\partial v}{\partial z}\right). \tag{4.27}$$

Eqs. (4.22)-(4.27) define a linear system for the unknowns S^{xx}, S^{yy}, S^{zz}, S^{xy}, S^{xz} and S^{yz} which is solved as follows. First, we assume that the initial condition **S**$=$**0** holds in which case from (4.24) we have $(S^{zz})^{(n+1)} = 0$. Then, integrating (4.26) and (4.27) over $[t_n, t_{n+1}]$

we find (after applying integration by parts and the *mean value theorem for integrals*)

$$\left(S^{xz}\right)^{(n+1)} = e^{-\frac{1}{We}\delta t}\left(S^{xz}\right)^{(n)} + \frac{\left(1+e^{-\frac{1}{We}\delta t}\right)}{2Re}\left[\left(\frac{\partial u}{\partial z}\right)^{(n)} - \left(\frac{\partial u}{\partial z}\right)^{(n+1)}\right], \qquad (4.28)$$

$$\left(S^{yz}\right)^{(n+1)} = e^{-\frac{1}{We}\delta t}\left(S^{yz}\right)^{(n)} + \frac{\left(1+e^{-\frac{1}{We}\delta t}\right)}{2Re}\left[\left(\frac{\partial v}{\partial z}\right)^{(n)} - \left(\frac{\partial v}{\partial z}\right)^{(n+1)}\right]. \qquad (4.29)$$

The values of $\left(S^{xx}\right)^{(n+1)}$, $\left(S^{yy}\right)^{(n+1)}$ and $\left(S^{yy}\right)^{(n+1)}$ are then obtained by integrating Eqs. (4.22), (4.23) and (4.25) over $[t_n, t_{n+1}]$ by the trapezoidal rule yielding

$$\left(S^{xx}\right)^{(n+1)} = e^{-\frac{1}{We}\delta t}\left(S^{xx}\right)^{(n)} + \delta t\left[\left(\frac{\partial u}{\partial z}\right)^{(n+1)}\left(S^{xz}\right)^{(n+1)} + e^{-\frac{1}{We}\delta t}\left(\frac{\partial u}{\partial z}\right)^{(n)}\left(S^{xz}\right)^{(n)}\right]$$
$$+ \frac{1}{2}\frac{We}{Re}\left[\left(\frac{\partial u}{\partial z}\right)^{(n)} + \left(\frac{\partial u}{\partial z}\right)^{(n+1)}\right]^2\left(1-e^{-\frac{1}{We}\delta t}\right), \qquad (4.30)$$

$$\left(S^{yy}\right)^{(n+1)} = e^{-\frac{1}{We}\delta t}\left(S^{yy}\right)^{(n)} + \delta t\left[\left(\frac{\partial v}{\partial z}\right)^{(n+1)}\left(S^{yz}\right)^{(n+1)} + e^{-\frac{1}{We}\delta t}\left(\frac{\partial v}{\partial z}\right)^{(n)}\left(S^{yz}\right)^{(n)}\right]$$
$$+ \frac{1}{2}\frac{We}{Re}\left[\left(\frac{\partial v}{\partial z}\right)^{(n)} + \left(\frac{\partial v}{\partial z}\right)^{(n+1)}\right]^2\left(1-e^{-\frac{1}{We}\delta t}\right), \qquad (4.31)$$

$$\left(S^{xy}\right)^{(n+1)} = e^{-\frac{1}{We}\delta t}\left(S^{xy}\right)^{(n)} + \frac{\delta t}{2}\left[\left(\frac{\partial u}{\partial z}\right)^{(n+1)}\left(S^{yz}\right)^{(n+1)} + e^{-\frac{1}{We}\delta t}\left(\frac{\partial u}{\partial z}\right)^{(n)}\left(S^{yz}\right)^{(n)}\right.$$
$$\left. + \left(\frac{\partial v}{\partial z}\right)^{(n+1)}\left(S^{xz}\right)^{(n+1)} + e^{-\frac{1}{We}\delta t}\left(\frac{\partial v}{\partial z}\right)^{(n)}\left(S^{xz}\right)^{(n)}\right]$$
$$+ \frac{1}{2}\frac{We}{Re}\left[\left(\frac{\partial u}{\partial z}\right)^{(n)} + \left(\frac{\partial u}{\partial z}\right)^{(n+1)}\right]\left[\left(\frac{\partial v}{\partial z}\right)^{(n)} + \left(\frac{\partial v}{\partial z}\right)^{(n+1)}\right]\left(1-e^{-\frac{1}{We}\delta t}\right). \qquad (4.32)$$

For rigid boundaries parallel to *xz*- and *yz*-planes, the equations for the components of tensor **S** are obtained in a similar manner. For more details on how the system (4.22)-(4.27) is solved see [44].

5 Time-step calculation

The explicit solution of the momentum equation leads to the following restrictions on the time-step size δt:

$$\delta t < \delta t_{\text{CFL}} = \max\left\{\frac{\delta x}{|u|}, \frac{\delta y}{|v|}, \frac{\delta z}{|w|}\right\}, \qquad (5.1)$$

$$\delta t < \delta t_{\text{VISC}} = \frac{Re}{2}\frac{\delta x^2\delta y^2\delta z^2}{\delta x^2\delta y^2 + \delta x^2\delta z^2 + \delta y^2\delta z^2}. \qquad (5.2)$$

The restriction δt_{CFL} is related to the CFL condition while δt_{VISC} represents the viscous restriction due to explicit discretization of the momentum equations.

Since we solve the momentum equations using the Euler implicit method we might expect that the viscous restriction on the time step to be unrestricted. However, Oishi et al. [40] found that this is true only for confined flows. A numerical study with the Euler implicit method applied to free surface flows showed that the gain in the time step size was little more than four times the size of δt_{VISC}. Moreover, in order to improve the viscous restriction it was found necessary to make the pressure calculation on the free surface implicit (see Section 4.1). So far, we have not been able to obtain a stability analysis for the implicit techniques presented in this paper. However, we expect a much larger time step can be employed in the calculations as follows.

Following Tomé and McKee [15], the time-step size selected is given by

$$\delta t = \text{FACT} * \min\{\text{FACT1} * \delta t_{\text{VISC}}, \text{FACT2} * \delta t_{\text{CFL}}\}, \tag{5.3}$$

where $0 < \text{FACT},\text{FACT1},\text{FACT2} \leq 1$. The factors FACT,FACT1,FACT2 appear as a conservative measure because the exact values of the velocities are not known and the analysis for δt_{VISC} was performed for simple confined flow situations. The implementation of these inequalities follows the procedure outlined in Tomé et al. [17].

Up to now, Freeflow3D has performed explicit calculations and typical values of the constants FACT, FACT1, FACT2 have been 0.3 for the constant FACT and 0.5 for both constants FACT1 and FACT2. However, if $Re < 1$ the relevant restriction on the time-step size is δt_{VISC} which depends on the mesh spacing and on the Reynolds number only. Thus, if the Reynolds number is very low the time-step is required to be so small as to make the explicit calculation infeasible. As of now, we have not been able to prove that the implicit method developed in this work can employ a time-step size based on the CFL condition (5.1) only. However, two-dimensional calculations (see Oishi et al. [40]) have shown that the restriction (5.2) can be improved by making $\text{FACT1} \gg 1$ so that a much larger time-step can be employed when computing low Reynolds number free surface flows with the implicit Euler scheme.

6 Validation results

The equations described in the previous sections were implemented into the Freeflow3D code [18] in order to simulate unsteady free surface flows of UCM fluids.

Let us consider the following fully developed velocity profile at the fluid entrance

$$w(x,y) = 2U\left[R^2 - \left(x^2 + y^2\right)\right]/R^2. \tag{6.1}$$

Then, introducing this profile into the constitutive equation (2.6) it can be easily verified

Figure 6: Description of the domain used for the simulation of the flow in a pipe.

that one obtains the following analytic solution:

$$S^{xx}(x,y) = S^{yy}(x,y) = S^{xy}(x,y) = S^{xz}(x,y) = S^{yz}(x,y) = 0, \tag{6.2}$$

$$S^{zz}(x,y) = 2\frac{We}{Re}\left[\left(\frac{\partial w}{\partial x}\right)^2 + \left(\frac{\partial w}{\partial y}\right)^2\right]. \tag{6.3}$$

To validate the numerical method described in the previous sections we simulated the flow in a pipe of radius R and length $10R$ (see Fig. 6) and compared the numerical solutions with the respective analytic solutions given by Eqs. (6.1) and (6.3). On the pipe exit and on the pipe walls, the appropriate conditions for the velocity were imposed (see Section 3) while the non-Newtonian tensor was calculated by the equations presented in Section 4.5. At the pipe entrance we assumed the analytic solutions given by Eqs. (6.1)-(6.3).

The following data were employed: $R=0.005$m, $U=1$ms^{-1}, $\mu=10$Pa s, $\rho=1000$kg m^{-3} and $\lambda=0.002$s, so $Re=\rho UL/\mu=0.5$ and $We=\lambda U/R=0.4$. In order to demonstrate the convergence of the method, mesh refinement was performed with mesh sizes $\delta x=\delta y=\delta z=0.167$ (mesh M0 – $12\times12\times60$ cells) and $\delta x=\delta y=\delta z=0.125$ (mesh M1 – $16\times16\times80$ cells) and $\delta x=\delta y=\delta z=0.100$ (mesh M2 – $20\times20\times100$ cells) and $\delta x=\delta y=\delta z=0.083$ (mesh M3 – $24\times24\times120$ cells), respectively.

The time-step constants used in these simulations were FACT = 0.2, FACT1 = 5.0 and FACT2 = 0.5.

The simulations started with the pipe empty and the fluid was injected at the inflow with the velocity given by Eq. (6.1) until it reached the outflow and steady state was established. Under steady state conditions, the velocity and the stress fields, at any cross section of the pipe, must have the same values as those imposed at the inflow.

Fig. 7 shows contour lines of the velocity w and the component S^{zz} at time $t=2$s. We can see that the contour lines are all parallel indicating that the steady state has been achieved.

The numerical solutions obtained for the velocity w and for the component of the non-Newtonian tensor S^{zz} at the cross section situated at the middle of the pipe ($z/R=5$) are shown in Fig. 8. We can see that there is good agreement between the numerical solutions obtained in the three meshes and the exact solution. These results validate the numerical technique presented in this paper. In addition, Table 1 presents the relative

(a)

(b)
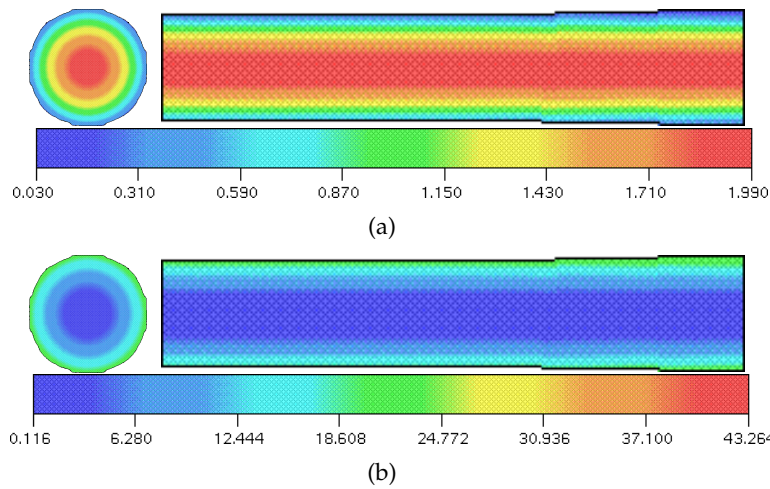
Figure 7: Visualization of w and S^{zz} along the pipe at time $t=2s$. Results shown at cross section $z/R=5$ and on the plane $y=0$, $0 \leq z/R \leq 10$, $-1 \leq x/R \leq 1$.

(a)

(b)
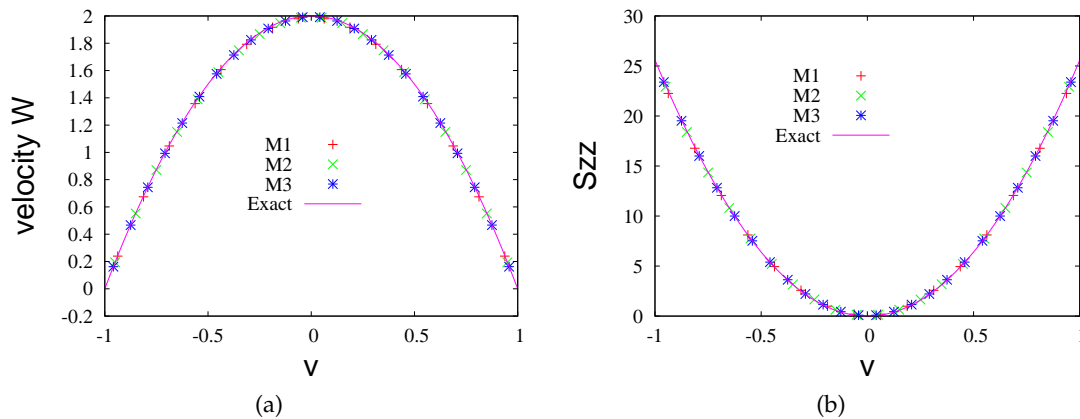
Figure 8: Numerical solutions obtained on meshes M1, M2, M3 at the middle of the pipe. The numerical and exact solutions were calculated at the line $x=0$, $-1 \leq y/R \leq 1$ and $z/R=5$. The results on mesh M0 are not shown for clarity.

errors obtained on the four meshes using the l_2-norm (see Eq. (6.5)) while Fig. 9 displays the diminishing of the errors as a function of mesh spacing. We can see in Table 1 that the errors decrease as the mesh is refined. This fact shows that the numerical method is convergent. Additionally, we used the data of Table 1 and calculated three estimates of the order of convergence for both the velocity w and the stress component S^{zz}. We employed the formula

$$N_i(\bullet) = \frac{\log\left(\frac{E(\bullet)_{M_{i+1}}}{E(\bullet)_{M_i}}\right)}{\log\left(\frac{\delta x_{M_{i+1}}}{\delta x_{M_i}}\right)}, \quad i=0,1,2, \tag{6.4}$$
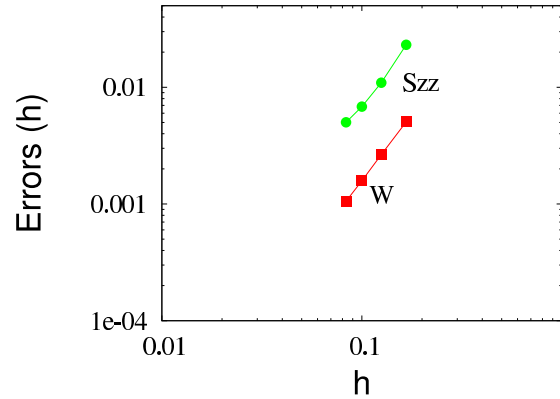
Figure 9: Decrease of the errors as a function of the mesh spacing h.

and found the following orders of convergence: $N_0(w) = 2.2$, $N_0(S_{zz}) = 2.6$, $N_1(w) = 2.3$, $N_1(S_{zz}) = 2.1$, $N_2(w) = 2.2$, $N_2(S_{zz}) = 1.7$. These results indicate that (for pipe flows at least) the numerical method is approximately second order accurate. Here

$$E = \sqrt{\frac{\sum_{i,j}(ExSol - NumSol)^2}{\sum_{i,j}(ExSol)^2}}, \qquad (6.5)$$

where *ExSol* and *NumSol* denote, respectively, the exact solution and the numerical solution.

Table 1: Errors obtained on the four meshes, using l_2-norm.

Mesh	M0	M1	M2	M3
$E(w)$	5.0547×10^{-3}	2.6494×10^{-3}	1.5804×10^{-3}	1.0563×10^{-3}
$E(S^{zz})$	2.3129×10^{-2}	1.0949×10^{-2}	6.8301×10^{-3}	5.0099×10^{-3}

7   Numerical results

To demonstrate that the numerical method presented in this paper can cope with viscoelastic free surface flows of UCM fluids we simulated the time-dependent problems of jet buckling (for details see Cruickshank and Munson [46]) and extrudate swell.

7.1   Jet buckling

The jet buckling phenomenon happens when a viscous jet flows onto a rigid plate where, soon after the jet impinges on the plate, the fluid decelerates causing the incoming fluid to accumulate. This problem has attracted the attention of many investigators and experimental/numerical results showing the buckling of three-dimensional Newtonian jets

can be found in the literature (e.g. Cruickshank and Munson [46], Castelo et al. [18], Ribe [19–21], Tomé et al. [22], Nóbrega et al. [23]).

To show that the technique developed in this work can simulate this problem for viscoelastic fluids, we performed two simulations using a UCM jet and compared the results with the equivalent results obtained with a Newtonian jet. The jets were issued vertically from an inlet of diameter $D=6$mm onto a square solid surface with dimensions 7cm $\times$ 7cm $\times$ 3mm. The vertical distance between the inlet and the solid surface was $H=12$cm and the computational mesh used had $70\times70\times128$ cells ($\delta x = \delta y = \delta z = 1$mm). We employed two types of jets: axisymmetric and square. The data employed in these simulations are displayed in Table 2. For the UCM fluid we had $We=\lambda U/D=0.5$ while the Reynolds numbers employed in the simulations were $Re=\rho UD/\mu=0.5$ and $Re=1.3$.

Table 2: Data used in the simulation of jet buckling.

$Re=0.5$	$Re=1.3$	common data
$U=0.5$m s^{-1}	$U=0.5$m s^{-1}	$H=0.12$m
$\mu=6$Pa s	$\mu=2.3077$Pa s	$D=0.006$m
$\lambda=0.006$s	$\lambda=0.006$s	$\rho=1000$kg m^{-3}

According to the experimental results of Cruickshank and Munson [46], axisymmetric Newtonian jets should buckle if both conditions $Re=\rho UD/\mu<1.2$ and $H/D>7.2$ are satisfied. In the simulations, we had $H/D=20$ and therefore we can expect that the Newtonian jet with $Re=0.5$ will buckle while the jet with $Re=1.3$ should not.

The Freeflow3D code ran these problems and the results obtained in these simulations are displayed in Figs. 10 and 11. We can see in Figs. 10 and 11 that for the case of $Re=0.5$ all jets produced the buckling phenomenon. Moreover, both Newtonian and UCM axisymmetric jets presented the known effect of coiling and a similar effect is also observed in the results obtained with the square jet. On the other hand, Figs. 12 and 13 show that the results corresponding to the case of $Re=1.3$: both axisymmetric and square Newtonian jets did not buckle (as predicted by Cruickshank's theory [46]). However, we can see in Figs. 12 and 13 that both UCM jets displayed the buckling effect (this is more pronounced in the results from the square jet in Figs. 13). We believe that the UCM jets buckled because of the high extensional viscosity developed after the jet impinged on the planar surface. Indeed, to emphasize this point we performed one additional simulation employing the axisymmetric jet. We used the same data shown in Table 2 for $Re=1.3$ except the parameter λ was increased to 0.0072s leading to a Weissenberg number of $We=\lambda U/D=0.6$. Fig. 14 displays the displacement of the jet surface at selected times. We can observe in Fig. 14 that a slight increase in the Weissenberg number made the jet buckle soon after it impinged onto the rigid surface. This suggests that viscoelasticity has a strong effect in the jet buckling phenomenon. Indeed, by using a Phan-Thien-Tanner fluid, Paulo et al. [48] have demonstrated that extensional viscosity plays a fundamental role in the jet buckling phenomenon.
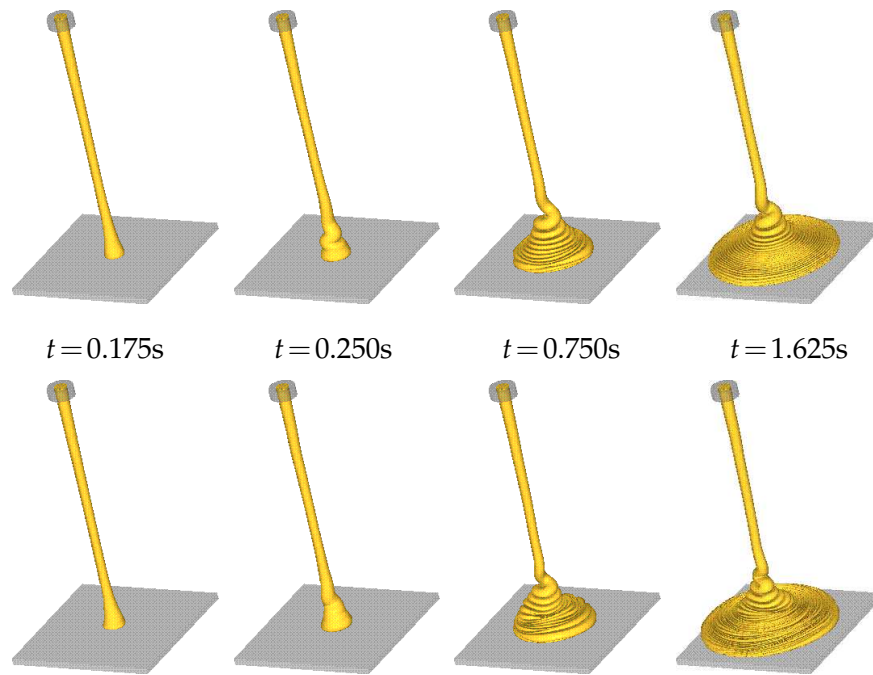
Figure 10: Numerical simulation of jet buckling of axisymmetric jets. First row: Newtonian jet with $Re\!=\!0.5$. Second row: UCM jet with $Re\!=\!0.5$ and $We\!=\!0.5$. Fluid flow visualization at selected times.
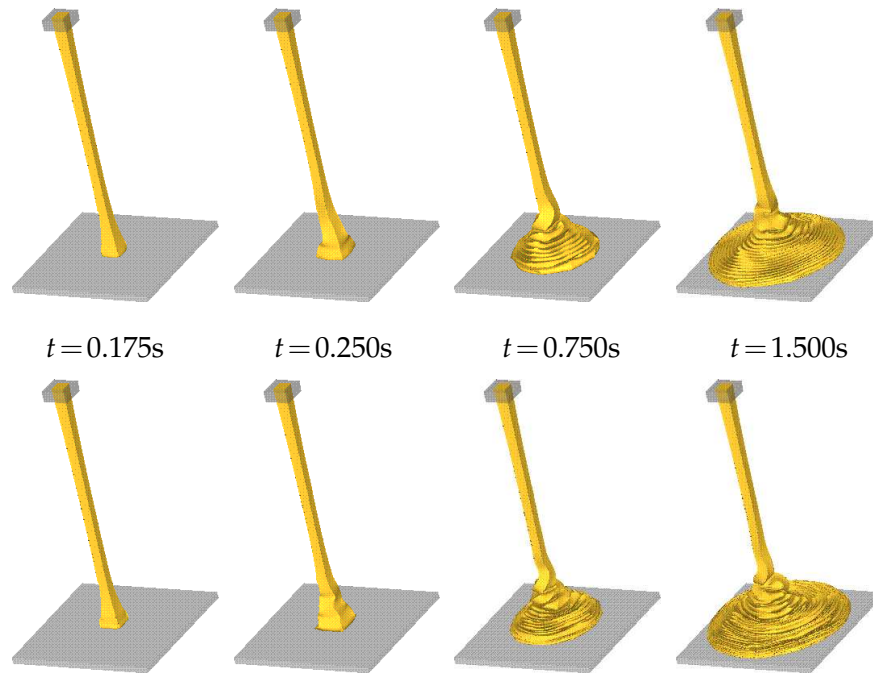
Figure 11: Numerical simulation of jet buckling of square jets. First row: Newtonian jet with $Re\!=\!0.5$. Second row: UCM jet with $Re\!=\!0.5$ and $We\!=\!0.5$. Fluid flow visualization at selected times.
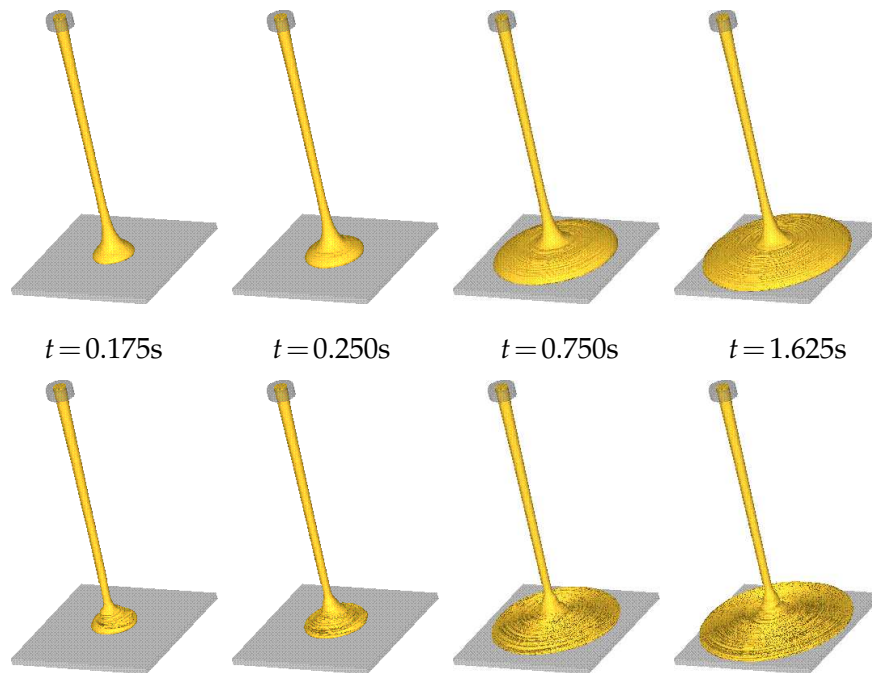
Figure 12: Numerical simulation of jet buckling of axisymmetric jets. First row: Newtonian jet with $Re = 1.3$. Second row: UCM jet with $Re = 1.3$ and $We = 0.5$. Fluid flow visualization at selected times.
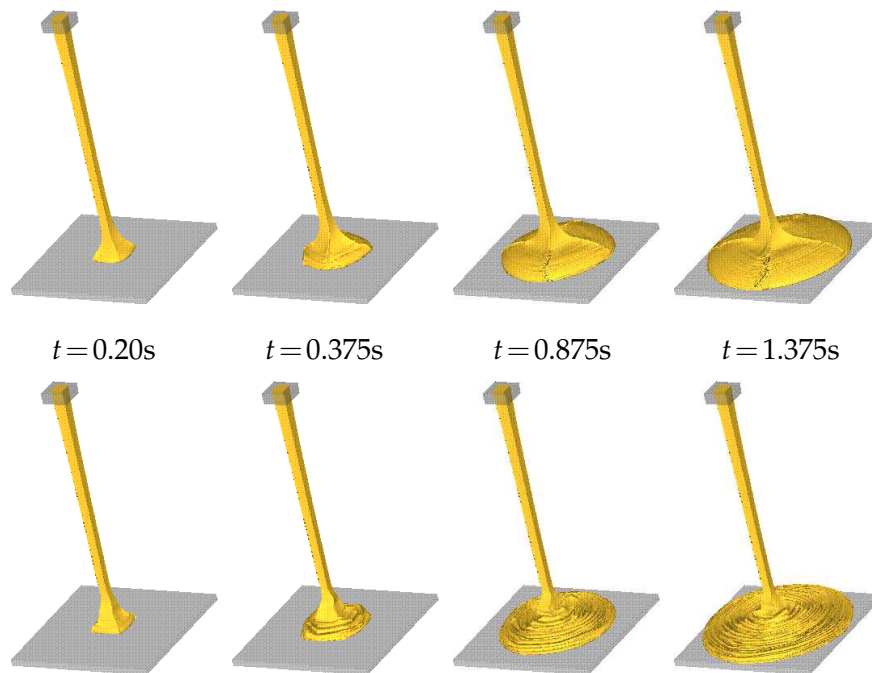
Figure 13: Numerical simulation of jet buckling of square jets. First row: Newtonian jet with $Re = 1.3$. Second row: UCM jet with $Re = 1.3$ and $We = 0.5$. Fluid flow visualization at selected times.
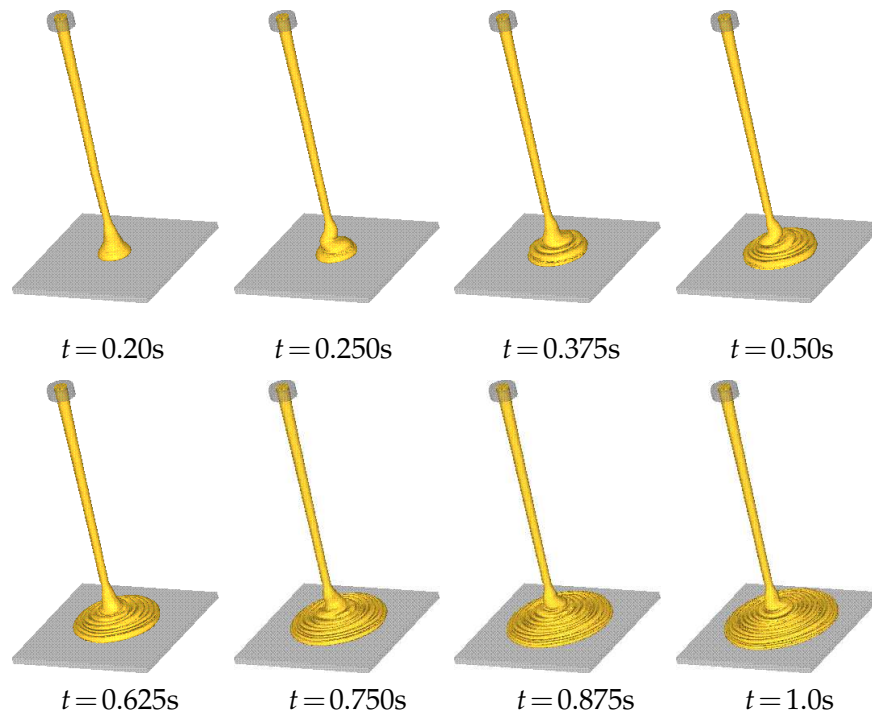
Figure 14: Numerical simulation of jet buckling of axisymmetric jets. UCM jet with $Re = 1.3$ and $We = 0.6$. Fluid flow visualization at selected times.

7.2 Numerical simulation of the transient extrudate swell

The extrudate swell phenomenon occurs when a jet issuing from a pipe with diameter D is extruded into the atmosphere where, due to normal stress differences, the jet swells attaining a new diameter D_{max} at some point downstream of the pipe exit. It is quantitatively characterized by the swelling ratio $S_r = D_{max}/D$. Due to its importance in industrial applications, the extrudate swell has been extensively investigated both experimentally (e.g., [49–52]) and numerically (e.g., [24, 48, 53–55]).

To simulate this problem, we considered a pipe with radius R and length $5R$. At the pipe entrance we imposed the fully-developed flow given by Eq. (6.1) while at the pipe walls the no-slip condition was employed. The simulations started with the pipe empty and the fluid was injected at the pipe entrance until it left the pipe and was extruded into the atmosphere. The extrudate swell phenomenon was then observed and analyzed. We used a computational domain of 3cm×3cm×10cm. To analyze the accuracy of the method we simulated this problem using the meshes M1 ($\delta x = \delta y = \delta z = 0.125$) and M2 ($\delta x = \delta y = \delta z = 0.100$) used in the validation results (see Section 6). Thus, in the mesh M1 we had $48 \times 48 \times 160$ cells while mesh M2 gave a total of $60 \times 60 \times 200$ cells. The interior of the pipe was covered by $16 \times 16 \times 40$ cells with mesh M1 while mesh M2 provided $20 \times 20 \times 50$ cells. The input data employed were $R = 0.5$cm, $U = 0.5$m s^{-1}, $\rho = 1000$kg m^{-3},
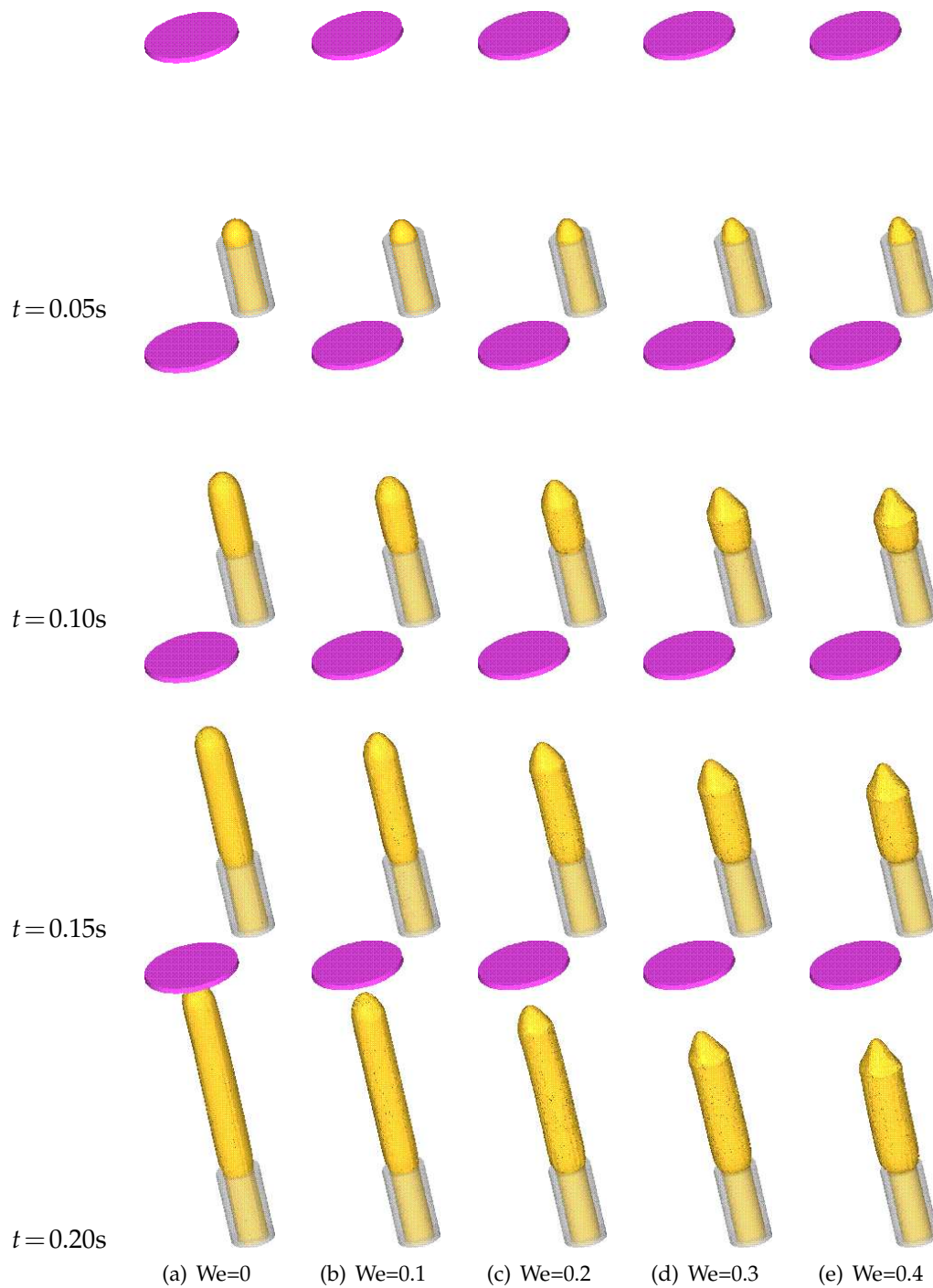
Figure 15: Numerical simulation of the extrudate swell for various Weissenberg numbers. Fluid flow visualization at different times. Results shown on mesh M1.

$\mu = 2.5\text{Pa s}$. Thus, $Re = \rho U R / \mu = 1$ for all simulations. The UCM relaxation time varied from $\lambda = 0.001\text{s}$ to $\lambda = 0.004\text{s}$, using 0.001s-step increments so that the Weissenberg number took the values $We = \lambda U / R = 0$ (Newtonian), 0.1, 0.2, 0.3 and 0.4, respectively. A total of ten simulations were performed.

Table 3: Time-dependent extrudate swell results using meshes M1 and M2. S_r predicted is obtained through the theory of Tanner [47].

	$We=0$	$We=0.1$	$We=0.2$	$We=0.3$	$We=0.4$
$U_{\min}$ (ms^{-1}) (M1)	0.436	0.385	0.356	0.288	0.262
$U_{\min}$ (ms^{-1}) (M2)	0.442	0.420	0.346	0.305	0.276
S_r obtained (M1)	1.098	1.113	1.188	1.310	1.375
S_r obtained (M2)	1.085	1.119	1.267	1.323	1.380
S_r predicted	1.130	1.143	1.177	1.225	1.277

The results of these simulations are displayed in Fig. 15 where we can observe that the greater is the Weissenberg number the larger is the swelling ratio S_r. Moreover, due to mass conservation, the velocity downstream from the pipe exit is reduced to a new value $U_{\min}$ that is inversely proportional to S_r. For the UCM fluid studied in this work, a theoretical value of S_r can be estimated by using the Tanner's law

$$S_r = 0.13 + \left[1 + 8We^2\right]^{1/6}$$

(see Tanner [47], see also a recent up-date of this work [56]). Table 3 shows the quantitative results obtained by the Marker-and-Cell approach described in this paper together with the predictions given by Tanner's formula. We can see in Table 3 that the results obtained on mesh M1 agree very well with those obtained on mesh M2. It can also be observed that for the range of Weissenberg numbers employed, the agreement with Tanner's law is quite good. It is, however, important to treat these results with great caution as the formula is based on gross over-simplification of the complex flow at the exit. Nevertheless, the results are relatively close to those obtained by Tomé et al. [48] for axisymmetric flows of an Oldroyd-B fluid.

8 Conclusions

This paper presented a finite difference method for simulating three-dimensional viscoelastic free surface flows of Upper-Convected Maxwell fluids. Fully developed flow in a three-dimensional pipe was simulated and the numerical results were compared with the analytic solutions; the agreement between them was good. Convergence results were obtained through mesh refinement. Numerical results presented included the time-dependent simulations of jet buckling and the extrudate swell phenomenon. In the case of jet buckling, it was observed that the UCM fluid does not obey the Cruickshank and Munson restrictions [46]. However, the swelling ratios obtained in the simulations of the

extrudate swell agreed qualitatively with Tanner's estimate [47] and were close to the numerical results obtained by the Oldroyd-B axisymmetric technique [48]. In summary, the numerical method was capable of simulating fully three-dimensional viscoelastic flows of UCM fluids with moving free surfaces.

Acknowledgments

References

[1] J. Yoo and Y. Na, A numerical study of the planar contraction flow of a viscoelastic fluid using the simpler algorithm, Journal of Non-Newtonian Fluid Mechanics, Vol. 30, pp. 89–106 (1991).

[2] E. Brasseur, M. Fyrillas, G. Georgiou and M. Crochet, The time-dependent extrudate-swell problem of an Oldroyd-B fluid with slip along the wall, Journal of Rheology, Vol. 42, pp. 549–566 (1998).

[3] J. Étienne, E.J. Hinch, J. Li, A Lagrangian-Eulerian approach for the numerical simulation of free-surface flow of a viscoelastic material, Journal of Non-Newtonian Fluid Mechanics, Vol. 136, pp. 157–166 (2006).

[4] J. Fang, R. G, Owens, L. Tacher, A. Parriaux, A numerical study of the SPH method for simulating transient viscoelastic free surface flows, Journal of Non-Newtonian Fluid Mechanics, Vol. 139, pp. 68–84 (2006).

[5] S. Kihara, T. Gouda, K. Matsunaga, K. Funatsu, Numerical simulation of three-dimensional viscoelastic flow within dies, Polymer Engineering & Science, Vol. 39, pp. 152–163 (2004).

[6] J. Ramirez, M. Laso, Micro-macro simulations of three-dimensional plane contraction flow, Modelling and Simulation in Materials Science and Engineering, Vol. 12, pp. 1293-1306 (2004).

[7] T. Yamamoto, M. Ishiyama, M. Nakajima, K, Nakamura, N. Mori, Three-dimensional viscoelastic flows through a rectangular channel with a cavity, Journal of Non-Newtonian Fluid Mechanics, Vol. 114, pp. 13–31 (2003).

[8] N. Fiétier, M. O. Deville, Simulations of time-dependent flows of viscoleastic fluids with spectral element methods, Journal of Scientific Computing, Vol 17, pp. 649–657 (2002)

[9] S. C. Xue, R. I. Tanner, N. Phan-Thien, Three-dimensional numerical simulation of viscoelastic flows - predictability and accuracy, Computer Methods in Applied Mechanics and Engineering, 180 305-331 (1999).

[10] G. Mompean and M. Deville, Unsteady finite volume of Oldroyd-b fluid through a three-dimensional planar contraction, Journal of Non-Newtonian Fluid Mechanics, Vol. 72, pp. 253–279 (1997).

[11] H. K. Rasmussen, O. Hassager, Three-dimensional simulations of viscoelastic instability in polymeric filaments, Journal of Non-Newtonian Fluid Mechanics, Vol. 82, pp. 189–202 (1999).

[12] J. M. Kim, K. H. Ahn, S. J. Lee, S. J. Lee, Numerical simulation of moving free surface problems in polymer processing using volume-of-fluid method, Polymer Engineering and Science, Vol. 41, pp. 856–866 (2001).

[13] A. Bonito, M. Picasso, M. Laso, Numerical simulation of 3d viscoelastic flows with free surface, Journal of Computational Physics, Vol. 215, pp. 691–716 (2006).

[14] F. H. Harlow and J. E. Welch, Numerical calculation of time-dependent viscous imcompressible flow of fluid with free surface, Physics of Fluids, Vol. 8, pp. 2182–2189 (1965).

[15] M. F. Tomé and S. McKee, GENSMAC: a computational marker-and-cell method for free surface flows, Journal of Computational Physics, Vol. 110, pp. 171–186 (1994).

[16] M. F. Tomé, B. R. Duffy and S. McKee, A numerical technique for solving unsteady Non-Newtonian free surface flows, Journal of Non-Newtonian Fluid Mechanics Vol. 62, pp. 9–34 (1996).

[17] M. F. Tomé, A. Castelo, J. A. Cuminato, N. Mangiavacchi and S. McKee, GENSMAC3D: A numerical method for solving three-dimensional free surface flows, International Journal for Numerical Methods in Fluids, Vol. 37, pp. 747–796 (2001).

[18] A. Castelo, M. F. Tomé, J. A. Cuminato, C. N. L. César and S. McKee, Freeflow: an integrated simulation system for three-dimensional free surface flows, Computing and Visualization in Science, Vol. 2, pp. 199–210 (2000).

[19] N. M. Ribe, A general theory of the dynamics of thin viscous sheets, Journal of Fluid Mechanics, Vol. 457, pp. 255–283 (2002).

[20] N. M. Ribe, Periodic folding of viscous jets, Physical Review E, Vol. 68, Art. No. 036305 Part 2 (2003).

[21] N. M. Ribe, Coiling of viscous jets, Proceedings of the Royal Society of London, Series A - Mathematical Physical and Engineering Sciences, Vol. 460, pp. 3223–3239 (2004).

[22] M. F. Tomé, L. Grossi, A. Castelo, J. A. Cuminato, N. Mangiavacchi, V. G. Ferreira, F. S. Sousa and S. McKee, A numerical method for solving three-dimensional generalized Newtonian free surface flows, Journal of Non-Newtonian Fluid Mechanics, Vol. 123, pp. 85–103 (2004).

[23] M. Nóbrega, O. S. Carneiro, F. T. Pinho, G. S. Paulo, M. F. Tomé, A. Castelo, J. A. Cuminato, The phenomenon of jet buckling: experimental results and numerical predictions, Proceedings of the Polymer Processing Society, 23rd Annual Meeting (2007), Salvador, Brasil.

[24] G. S. Paulo, M. F. Tomé and S. McKee, A marker-and-cell approach to viscoelastic free surface flows using the PTT model, Journal of Non-Newtonian Fluid Mechanics, Vol. 147, pp. 149–174 (2007).

[25] M. F. Tomé, A. Castelo, V. G. Ferreira and S. McKee, A finite difference technique for solving the Oldroyd-B model for 3D-unsteady free surface flows, Journal of Non-Newtonian Fluid Mechanics, Vol. 154, pp. 179–206 (2008).

[26] D. Rajagopalan, R. C. Armstrong and R. A. Brown, Finite element methods for calculation of steady, viscoelastic flow using constitutive equations with a Newtonian viscosity, Journal of Non-Newtonian Fluid Mechanics, Vol. 36, pp. 159–192 (1990).

[27] M. Crochet, A. R. Davis and K. Walters, Numerical simulation of Non-Newtonian flow, Elsevier (1984).

[28] G. K. Batchelor, An Introduction to Fluid Dynamics, Cambridge University Press (1967).

[29] H. Miyata and S. Nishimura, Finite-diference simulation of nonlinear waves generated by ships of arbitrary three-dimensional configuration, Journal of Computational Physics, Vol.

60, pp. 391-436 (1985).

[30] C. Lemos, Higher-order schemes for free surface flows with arbitrary configurations, International Journal for Numerical Methods in Fluids, Vol. 23, pp. 545-566 (1996).

[31] B. D. Nichols, C. W. Hirt and R. S. Hotchkiss, SOLA-VOF: A solution algorithm for transient fluid flow with multiple free boundaries, Los Alamos Scientific Laboratory, Technical Report LA-8355 (1988).

[32] V. Armenio, An improved MAC method (SIMAC) for unsteady high-Reynolds free surface flows, International Journal for Numerical Methods in Fluids, Vol. 24, pp. 185–214 (1997).

[33] A. J. Chorin, Numerical solution of the Navier-Stokes equations, Journal of Computational Physics, Vol. 2, pp. 745–762 (1968).

[34] J. B. Bell, P. Colella and H. M. Glaz, A second-order projection method for the incompressible Navier-Stokes equations, Journal of Computational Physics, Vol. 85, pp. 257–283 (1989).

[35] D. L. Brown, R. Cortez, and M. L. Minion, Accurate projection methods for the incompressible Navier-Stokes equations, Journal of Computational Physics, Vol. 168, pp. 464–499 (2001).

[36] H. Johnston and J. G. Liu, Accurate, stable and efficient Navier-Stokes solvers based on explicit treatment of the pressure term, Journal of Computational Physics, Vol. 199, pp. 221–259 (2004).

[37] W. Kress and P. Lotstedt, Time step restrictions using semi-explicit methods for incompressible Navier-Stokes equations, Computer Methods in Applied Mechanics and Engineering, Vol. 195, pp. 4433–4447 (2006).

[38] C. M. Oishi, M. F. Tomé, J. A. Cuminato, S. McKee, An implicit technique for solving 3D low Reynolds number moving free surface flows, Journal of Computational Physics, Vol. 227, pp. 7446–7468 (2008).

[39] F. S. de Sousa, N. Mangiavacchi, L. G. Nonato, A. Castelo, M. F. Tomé, V. G. Ferreira, J. A. Cuminato and S. McKee, A front-tracking/front-capturing method for the simulation of 3D multi-fluid flows with free surfaces, Journal of Computational Physics, Vol. 198, pp. 469–499 (2004).

[40] C. M. Oishi, J. A. Cuminato, V. G. Ferreira, M. F. Tomé, A. Castelo, N. Mangiavacchi and S. McKee, A stable semi-implicit method for free surface flows, Transactions of ASME Journal of Applied Mechanics, Vol. 73, pp. 940–947 (2006).

[41] M. Alves, P. Oliveira, and F. T. Pinho, A convergent and universally bounded interpolation scheme for the treatment of advection, International Journal for Numerical Methods in Fluids, Vol. 41, pp. 47–75 (2003).

[42] V. G. Ferreira, A. C. Brandi, F. A. Kurokawa, P. Seleghim, A. Castelo and J. A. Cuminato, Incompressible turbulent flow simulation using k-e model and upwind schemes, Mathematical Problems in Engineering, Vol. 2007, pp 1–26 (2007).

[43] M. F. Tomé, N. Mangiavacchi, J. A. Cuminato, A. Castelo and S. McKee, A numerical technique for solving unsteady viscoelastic free surface flows, Journal of Non-Newtonian Fluid Mechanics Vol. 106, pp. 61–106 (2002).

[44] R. A. P. Silva, Solução Numérica do Modelo de Maxwell para Escoamentos Tridimensionais com Superfícies Livres, MSc Thesis, ICMC-USP, (2007).

[45] V. G. Ferreira, M. F. Tomé N. Mangiavacchi, A. Castelo, J. A. Cuminato, A. O. Fortuna and S. McKee, High-order upwinding and the hydraulic jump, International Journal for Numerical Methods in Fluids, Vol. 39, pp. 549–583 (2002).

[46] J. O. Cruickshank and B. R. Munson, Viscous fluid buckling of plane and axisymmetric jets, Journal of Fluid Mechanics Vol. 113, pp. 221–239 (1981).

[47] R. I. Tanner, A theory of die-swell, J. Polymer Science Vol. 8, pp. 2067–2078 (1970).

[48] M. F. Tomé, L. Grossi, A. Castelo, J. A. Cuminato, S. McKee and K. Walters, Die-swell, splashing drop and a numerical technique for solving the Oldroyd-B model for axisymmetric free surface flows, Journal of Non-Newtonian Fluid Mechanics, Vol. 141, pp. 148–166 (2007).

[49] A. L. N. Silva, M. C. G. Rocha, F. M. B. Coutinho, Study of rheological behavior of elastomer/polypropylene blends, Polymer Testing, Vol. 21, pp. 289-293 (2002).

[50] J-Z. Liang, Estimation of melt shear modulus from extrudate swell ratio and exit-pressure drop data, Journal of Thermoplastic Composite Materials, Vol. 17, pp. 545-556 (2004).

[51] Y. Liang, A. Ozetkin, and S. Neti, Dynamics of viscoelastic jets of polymeric liquid extrudate, Journal of Non-Newtonian Fluid Mechanics, Vol. 81, pp. 105-132 (1999).

[52] N. Sombatsompop, N.-T. Intawong, A comparative study on extrudate swell ratio of polystyrene in a capillary rheometer and a single screw extruder, Polymer Testing, Vol 24, pp. 948-952 (2005).

[53] S. X. Huang, C. J. Lu, Stress relaxation characteristics and extrudate swell of the IUPAC-LDPE melt, Journal of Non-Newtonian Fluid Mechanics, Vol. 136, pp. 147-156 (2006).

[54] R. P. G. Rutgers, M. R. Mackley, The effect of channel geometry and wall boundary conditions on the formation of extrusion surface instabilities for LLDPE, Journal of Non-Newtonian Fluid Mechanics, Vol. 98, pp. 185-199 (2001).

[55] E. Mitsoulis, Three-dimensional non-Newtonian computations of extrudate swell with the finite element method, Computer Methods in Applied Mechanics and Engineering, Vol. 180, pp. 333-344 (1999).

[56] R. I. Tanner, A theory of die-swell revisited, Journal of Non-Newtonian Fluid Mechanics, Vol. 129, pp. 85-87 (2005).